PHYSICAL REVIEW A **113**, 033304 (2026)

Thermodynamics and Tomonaga-Luttinger liquid behavior of the quantum one-dimensional hard-rod model

Shengjie Yu,[1,*] Zhaoxuan Zhu,[2] and Laurent Sanchez-Palencia[1]
[1] *CPHT, CNRS, Ecole Polytechnique, IP Paris, F-91128 Palaiseau, France*
[2] *Beijing National Laboratory for Condensed Matter Physics, Institute of Physics, Chinese Academy of Sciences, Beijing 100190, China*

(Received 27 May 2025; accepted 4 February 2026; published 5 March 2026)

The one-dimensional hard-rod model describes impenetrable bosons with finite diameter, extending the Lieb-Liniger model to systems with excluded volume interactions. Here, we investigate the thermodynamics of quantum hard rods using Yang-Yang theory, path integral quantum Monte Carlo calculations, and Tomonaga-Luttinger liquid theory. We first discuss the behavior of characteristic thermodynamic quantities, exhibiting deviations to the Lieb-Liniger model for sufficiently high densities, with excellent agreement between analytical and numerical results. We then show that the hard-rod model exhibits Tomonaga-Luttinger liquid behavior across a wide range of parameters, at zero and finite temperature, as unveiled by correlation functions. The Luttinger parameter and thermal length can be extracted by fitting correlation functions to Tomonaga-Luttinger liquid theory, hence demonstrating a robust method for thermometry. This work provides a comprehensive study of strongly correlated hard-rod systems at finite temperatures, with applications to quantum wires, spin chains, and ultracold atoms.

DOI: 10.1103/8gzf-v52y

I. INTRODUCTION

Hard-sphere models describe hard-core particles with a finite diameter. They form a central class of classical statistical models for modeling universal thermodynamic properties of repulsive particle gases, with applications to liquid-gas transitions and fluid dynamics [1–6], as well as generalized hydrodynamics [7–11]. Classical models, as well as their quantum counterparts, have been extensively studied with direct applications to rigid molecules and colloidal systems [12], strongly repulsive particles in gaseous helium on carbon nanotubes [13,14], spin-ion compounds [15], polarized hydrogenoids [16], and ultracold atoms [17–22]. Notably, hard spheres are also reminiscent of the excluded volume associated with Rydberg blockade in atomic systems [23]. In one dimension (1D), the hard-rod (HR) model is a natural extension of the Lieb-Liniger model, which describes one-dimensional bosons with contact interactions [24,25].

In quantum systems, the reduced dimensionality exaggerates quantum correlations, leading to unique phenomena in 1D, such as the absence of Bose-Einstein condensation, fermionization of interacting Bose gases, and the breakdown of quasiparticle excitations [26,27]. Quantum systems in 1D are also highly susceptible to perturbations with characteristic lengths commensurate with the average interparticle distance, leading to the celebrated pinning transition in arbitrary weak periodic potentials [28–30] and Bose glass transitions in disordered or quasiperiodic systems [31–37]. Unlike in three dimensions, quantum correlations in one-dimensional bosonic systems increase with decreasing particle density, making them an ideal test bed for studying strongly correlated regimes in dilute systems. This applies to a variety of physical systems, including electronic quantum wires, spin chains, organic conductors, and tightly confined ultracold atoms [26,27]. Recent experimental observations have confirmed a number of phenomena, such as Tonks-Girardeau (TG) physics [38,39], absence of thermalization in integrable systems [40], spin-charge separation [41,42], Mott transitions in shallow periodic potentials [43,44], disorder-induced enhancement of coherence [45], and the observation of the Tan contact [46,47].

Another asset of quantum one-dimensional systems is that they are particularly suited to exact or quasiexact theoretical approaches. Most of their properties are captured by the universal harmonic fluid theory, known as Tomonaga-Luttinger liquids (TLL) [48–50]. The latter predicts algebraically decaying correlation functions with exponents determined by the sole TLL parameter, which is, however, model dependent. Moreover, quantum one-dimensional systems are amenable to quasiexact numerical approaches based on tensor-network representations [51–53]. Last but not least, 1D offers a variety of exactly solvable strongly correlated quantum models, including the celebrated Lieb-Liniger (LL) model [24,25] and a number of descendents [54].

The HR model has been previously studied in several works. The standard approach for the ground state involves mapping onto the LL model with infinite repulsive interactions (TG gas) by excluding the volume occupied by the HRs and shifting the ordered coordinates of the particles accordingly [55]. Beyond the ground state, more advanced approaches are required. The Bethe ansatz (BA) and thermodynamic Bethe ansatz (TBA) solutions have been derived in Refs. [56–59]. Moreover, the dynamical structure factor and

---

[*] Contact author: ysj2pwp@gmail.com

TLL behavior of HRs have been studied at zero temperature using variational Monte Carlo [18,60].

In this work, we extend these studies to finite temperatures. We first briefly review the BA and TBA solutions for the HRs. Then, we perform quantum Monte Carlo (QMC) calculations at finite temperatures, finding excellent agreement with the exact TBA solutions. We also compute one- and two-body correlation functions and find results in excellent agreement with TLL behavior. The unknown coefficients from the TLL theory are then extracted from fits to the QMC results. We show that using these fits, the universal properties of TLL allow for a thermometry of one-dimensional systems described by HRs. In addition, we discuss the behavior of the static structure factor, which displays nonanalytical peaks at zero temperature and power-law scaling of the peaks as a function of temperature. Finally, possible applications to Rydberg atom systems are outlined.

II. BETHE ANSATZ SOLUTION

We first briefly review the BA solution for the ground state (GS) and excitations. Similar derivations were first presented in Refs. [56–59] (see also Ref. [60]). The Hamiltonian for one-dimensional bosons with pairwise interactions is given by

$$\hat{H} = -\frac{\hbar^2}{2m}\sum_{j=1}^{N}\frac{\partial^2}{\partial x_j^2} + \sum_{\ell>j} V(x_\ell - x_j), \tag{1}$$

where m is the particle mass, N is the total number of particles, and x_j denotes the center position of particle j. Equation (1) describes a family of models determined by the scattering potential $V(x)$. For HRs, it reads as $V(x) = \infty$ for $|x| \leqslant a$ and $V(x) = 0$ for $|x| > a$, which describes impenetrable particles with finite diameter a.

The BA wave function is written as

$$\Psi(\mathbf{x}) = \sum_{\mathcal{P}\in S_N} A_{\mathcal{P}} \exp\left(i\sum_{j=1}^{N} k_{\mathcal{P}_j} x_j\right), \tag{2}$$

for $|x_{j+1} - x_j| \geqslant a$, and $\Psi(\mathbf{x}) = 0$ otherwise. The latter guarantees the HR impenetrability condition, which forces the distance between consecutive particles to exceed a. Here, S_N is the symmetric group over $\{1, \ldots, N\}$, and $\mathbf{x} = (x_1, \ldots, x_N)$ represents the ordered particle coordinates. Since $\Psi(\mathbf{x})$ vanishes for $x_{j+1} - x_j < a$, the energy is fully kinetic and reads as $E = \sum_j \hbar^2 k_j^2/2m$. To determine the coefficients $A_{\mathcal{P}}$ and quasimomenta k_j, the continuity condition requires the wave function to vanish at the HR boundaries, i.e.,$\Psi(x_1, \ldots, x_j, x_j + a, \ldots, x_N) = 0$, for all $j \in \{1, \ldots, N\}$. It yields the relations $A_{(j,j+1)\mathcal{P}} = -e^{i\Theta(k_{\mathcal{P}_{j+1}} - k_{\mathcal{P}_j})} A_{\mathcal{P}}$, for any j, where $\Theta(k) = ka$ is the phase shift of two-body scattering, defined in the same way as the Lieb-Liniger model. These equations are solved by

$$A_{\mathcal{P}} = (-1)^{\mathcal{P}} A \exp\left[-i\sum_j k_{\mathcal{P}_j}(j-1)a\right]. \tag{3}$$

Periodic boundary conditions (PBCs) then yield the BA equation

$$k_j L = 2\pi I_j + \sum_{\ell\neq j}\Theta(k_j - k_\ell) \tag{4}$$

for any $j \in \{1, \ldots, N\}$, where the quantum numbers I_j take integer or half-integer values for odd or even N, respectively. The parity of N contributes since the PBCs involve $(N-1)$ interchanging of momenta, leading to a phase of $(N-1)\pi$. The set of N quantum numbers $\{I_j\}$ characterizes the eigenstate uniquely. For HRs, the linear form of $\Theta(k)$ allows for an explicit solution. By summing all Eqs. (4) for all j's, one finds the total momentum $Q = \sum_j k_j = 2\pi I/L$, with $I = \sum_j I_j$. Then, inserting this formula for Q and $\Theta(k) = ka$ into Eq. (4), one finds

$$k_j = \frac{2\pi I_j - 2\pi I a/L}{L - Na}, \quad I = \sum_j I_j. \tag{5}$$

Note that the dimensionless quantities $k_j a$ and $Ea^2m/\hbar^2$ are universal functions of a/L and N. The TG gas, which describes infinitely repulsive, pointlike particles, is found in the limit $a \to 0$, and we recover the known solution $k_j^{\mathrm{TG}} = 2\pi I_j/L$ [61].

A. Ground state

The ground state is obtained by minimizing the energy. The quadratic form of the latter implies that the set of quasimomenta k_j should be symmetric, and the total momentum $Q = \sum_j k_j = 2\pi I/L$ should vanish, i.e., $Q = 0$ and $I = 0$. The quantum numbers I_j take all integer or half-integer values in the set $\{-\frac{N-1}{2}, \ldots, \frac{N-1}{2}\}$, hence creating a Fermi-like sea with maximum momentum $k_{\max} = \pi n/(1 - na)$, where $n = N/L$ is the particle density, in the thermodynamic limit. The energy per particle is then

$$\frac{E_0}{N} \approx \frac{\hbar^2\pi^2 n^2}{6m(1-na)^2}. \tag{6}$$

Compared to the TG gas, the quasimomenta are rescaled as $k_j = k_j^{\mathrm{TG}}/(1 - na)$ and the energy as $E_0 = E_0^{\mathrm{TG}}/(1 - na)^2$. The energy divergence at $na = 1$ is due to the complete impenetrability of HRs, which implies the condition $Na \leqslant L$, i.e.,$na \leqslant 1$ in the thermodynamic limit. Note, however, that the zero-temperature chemical potential, $\mu = \partial E_0/\partial N$, is rescaled differently, due to the dependence of the energy rescaling on the total particle number N. One finds

$$\mu = \frac{\hbar^2\pi^2 n^2}{2m}\frac{1 - na/3}{(1 - na)^3}, \tag{7}$$

i.e.,$\mu = \mu^{\mathrm{TG}}(1 - na/3)/(1 - na)^3$ with $\mu^{\mathrm{TG}} = \hbar^2\pi^2 n^2/2m$, the chemical potential of the TG gas.

B. Excitation spectrum

As usual in BA, elementary excitations are generated by changing one of the I_j's, creating two distinct branches [24,25]. Particle-type excitations (p, upper branch) are created by promoting a particle from the highest populated momentum $k_N = k_{\max}$ to a larger value $q > k_{\max}$ while hole-type excitations (h, lower branch) involve moving a particle from within the range of populated momenta to just above the largest quasimomentum. In both cases, although a single quantum number I_j is changed, all quasimomenta are shifted since I turns from 0 to $\neq 0$ [see Eq. (5)]. Although the shift is infinitesimal in the thermodynamic limit, it plays a crucial role because it affects all the momenta and has a macroscopic impact [60].

Adding a particle or a hole implies adding or removing a quasimomentum $\pm q_0$ and shifting the other quasimomenta so that $k' \to k' + f_{\mathrm{p,h}}(k')$. The total momentum for a particle or hole excitation then reads as

$$q = \pm q_0 + \int_{-k_{\max}}^{k_{\max}} J_{\mathrm{p,h}}(k')\mathrm{d}k', \tag{8}$$

where the plus and minus signs correspond to the particle and hole types, respectively, and the energy as

$$\varepsilon_{\mathrm{p,h}}(q) = \pm\left(\frac{\hbar^2 q_0^2}{2m} - \mu\right) + \frac{\hbar^2}{2m}\int_{-k_{\max}}^{k_{\max}} 2kJ_{\mathrm{p,h}}(k')\mathrm{d}k', \tag{9}$$

where the chemical potential μ compensates the energy of adding or removing a particle and $J_{\mathrm{p,h}}(k) = \rho(k) f_{\mathrm{p,h}}(k)L$ is the density of quasimomentum shift, where $\rho(k)$ is the density of quasimomenta in the ground state. The latter is determined using Eq. (4), which yields the self-consistent equation

$$\begin{aligned} 2\pi J_{\mathrm{p,h}}(k) = &-\int_{-k_{\max}}^{k_{\max}} \mathcal{K}(k-k')J_{\mathrm{p,h}}(k')\mathrm{d}k' \\ &\mp [\pi + \Theta(q_0 - k)], \end{aligned} \tag{10}$$

with $\mathcal{K}(k) = \mathrm{d}\Theta/\mathrm{d}k$. For HRs, the constant kernel, $\mathcal{K}(k) = a$, allows again for an analytical solution,

$$J_{\mathrm{p,h}}(k) = \mp\frac{(1-na)(q_0 a + \pi) - ka}{2\pi}. \tag{11}$$

Inserting this result into Eqs. (8) and (9), we find the analytic expressions

$$q = \pm(1-na)(q_0 - k_{\max}) \tag{12}$$

and

$$\varepsilon_{\mathrm{p,h}}(q) = \frac{\hbar^2 q(2\pi n \pm q)}{2m(1-na)^2}, \tag{13}$$

for the momentum and energy, respectively. We hence recover the results in Refs. [59,60]. The dispersion relations of the elementary excitations for the HR and TG models at $na = 0.2$ are shown in Fig. 1. Both models exhibit qualitatively similar behaviors but significant quantitative differences. The TG model is recovered from Eq. (13) for $a \to 0$, and, for HRs, the same energy rescaling $\varepsilon_{\mathrm{p,h}}(q) = \varepsilon^{\mathrm{TG}}_{\mathrm{p,h}}(q)/(1-na)^2$ as for the ground state. In particular, the hole branch has a momentum cutoff at the Fermi momentum $k_{\mathrm{F}} = \pi n$, for both HR and TG models.

III. THERMODYNAMICS

We now turn to the thermodynamics of the HR model at finite temperature. The different rescalings of the elementary excitation energies and chemical potential with na implies that no such simple rescaling can be applied here and a complete TBA approach must be derived [56–59]. This will allow one to determine the thermodynamics of the model and benchmark QMC calculations.

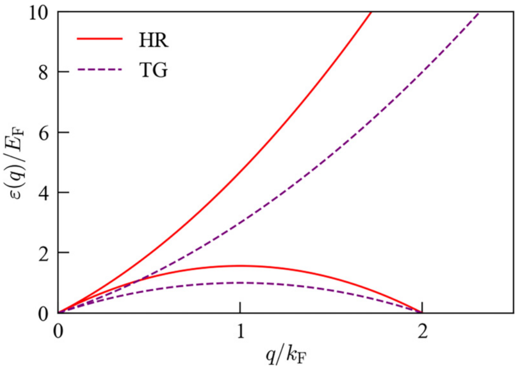

FIG. 1. Dispersion relation of elementary particle (upper branch) and hole (lower branch) excitations for the HR (solid red line) and the TG (dashed purple line) models at $na = 0.2$. Here $E_{\mathrm{F}} = \pi^2\hbar^2 n^2/2m$ is the Fermi energy.

To write the TBA of the HR model, we work along the lines of Yang and Yang [62]. In brief, we define $\rho(k)$ as the density of filled quasimomenta and $\rho_h(k)$ the density of holes, subject to the normalization condition

$$\rho(k) + \rho_h(k) = \frac{1}{2\pi} - \frac{1}{2\pi}\int_{-\infty}^{\infty} \mathcal{K}(k-k')\rho(k')\mathrm{d}k', \tag{14}$$

where $\mathcal{K}(k) \equiv \mathrm{d}\Theta/\mathrm{d}k = a$. Minimizing the free energy written in terms of the dressed energy,

$$\epsilon(k) \equiv k_B T\, \ln[\rho_h(k)/\rho(k)], \tag{15}$$

one finds the self-consistent Yang-Yang equation [58,59]

$$\begin{aligned} \epsilon(k) = &-\mu + \frac{\hbar^2 k^2}{2m} + k_{\mathrm{B}}T\int \frac{\mathrm{d}k'}{2\pi}\mathcal{K}(k-k') \\ &\times \ln[1 + e^{-\epsilon(k')/k_{\mathrm{B}}T}]. \end{aligned} \tag{16}$$

This equation is solved numerically for $\epsilon(k)$ using an iterative method. The latter is significantly simplified for HRs compared to the Lieb-Liniger model by the fact that $\mathcal{K}$ is a constant, which lifts the k dependence of the integral in Eq. (16) (see Appendix A for details). Then, using the numerical result for $\epsilon(k)$ in Eqs. (14) and (15), we find $\rho(k)$ and $\rho_h(k)$, as well as the free energy

$$F = N\mu - L\int \frac{\mathrm{d}k}{2\pi}\ln[1 + e^{-\epsilon(k)/k_{\mathrm{B}}T}]. \tag{17}$$

The particle density $n = \int_{-\infty}^{\infty}\mathrm{d}k\,\rho(k)$ is found from Eq. (14), which reduces to $\rho(k) + \rho_h(k) = (1-na)/2\pi$, leading to

$$na = \frac{\chi_2(\mu,T)}{1+\chi_2(\mu,T)}, \tag{18}$$

with $\chi_2(\mu,T) = a\int_{-\infty}^{\infty}\frac{\mathrm{d}k}{2\pi}\frac{1}{1+e^{\epsilon(k)/k_{\mathrm{B}}T}}$. This formula may be used to compute the compressibility using the standard thermodynamic relation,

$$\kappa \equiv \left(\frac{\partial n}{\partial\mu}\right)_T = \frac{(1-na)^3\chi_3(\mu,T)}{k_{\mathrm{B}}Ta}, \tag{19}$$

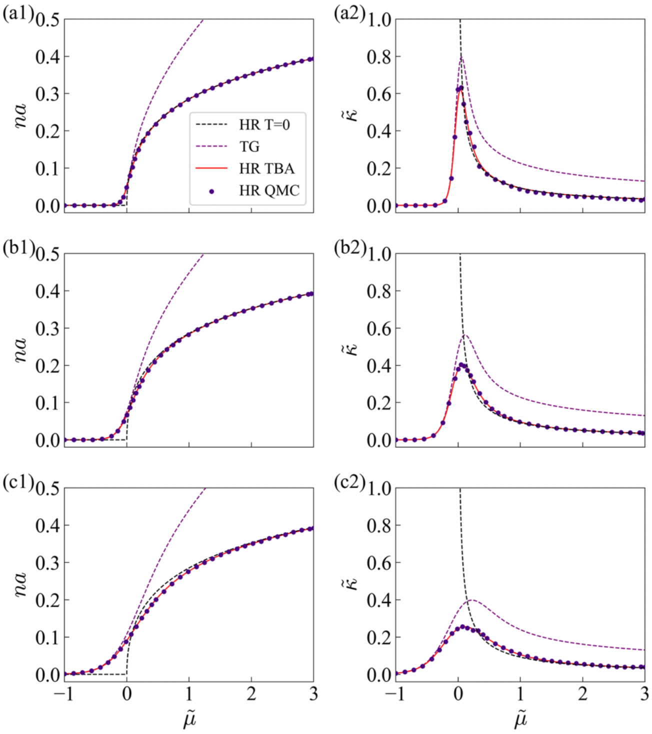

FIG. 2. Thermodynamics of HRs. (a) Rescaled density, na, and (b) compressibility, $\tilde{\kappa} = \hbar^2\kappa/ma$, vs chemical potential, $\tilde{\mu} = \mu ma^2/\hbar^2$, for the HR and TG models. For HRs, we show TBA predictions (solid red line) and QMC results (purple disks) at $(ma^2k_B/\hbar^2)T = 0.05,\ 0.1$, and 0.2 from top to bottom, as well as BA predictions at $T = 0$ (dashed black line). For TG gas, we show TBA predictions (dashed purple line). Error bars are smaller than the size of markers and the width of lines.

with $\chi_3(\mu, T) = a\int_{-\infty}^{\infty}\frac{\mathrm{d}k}{2\pi}\frac{e^{\epsilon(k)/k_BT}}{(1+e^{\epsilon(k)/k_BT})^2}$. Both Eqs. (18) and (19) are explicitly derived in Appendix B. They provide characteristic quantities of the HR gas, namely, the equation of state and the compressibility, respectively. Other thermodynamic quantities, not discussed hereafter, are similarly found from derivatives of the free energy.

Then we turn to QMC simulations, as these provide us with more information than BA does, such as correlation functions. First of all, we benchmark the QMC against the exact TBA results. Our implementation works in the grand canonical ensemble with fixed temperature and chemical potential, and worm-algorithm updates [63]. The specific propagator for the HR interaction is given in Appendix C. Figure 2 shows the density na in the left column and the compressibility $\tilde{\kappa} = \kappa\hbar^2/ma$ in the right column versus chemical potential for various temperatures. QMC results are shown for the HRs (purple disks) while TBA predictions are shown for the HRs [solid red lines, Eqs. (18) and (19)] and for the TG model (dashed purple line). The thermodynamics of the TG gas is obtained by plugging $a = 0$ into the Yang-Yang equation (16), which directly yields $\epsilon(k) = -\mu + \hbar^2k^2/2m$. Then we compute the density and the compressibility from Eqs. (18) and (19), respectively. To circumvent the singularity at $a = 0$, we compute χ_2/a and χ_3/a. Note that for the TG gas, the density n is finite but na vanishes since $a = 0$. Hence, in Fig. 2, the plotted data for the TG gas is na with a the radius of the HRs considered in the same figure. The zero-temperature behavior, predicted by BA, is also shown for the HR model [dashed black lines, from Eq. (7)]. QMC results show excellent agreement with TBA across all chemical potentials and finite temperatures, confirming the TBA predictions. Moreover, the scaling of QMC results for decreasing temperatures confirm the $T = 0$ behavior predicted by BA. Qualitatively similar results are found for all temperatures except for $T = 0$.

At zero temperature, the density exhibits a sharp edge, $n \propto \sqrt{\mu}$, consistent with Eq. (7) in the limit $n \to 0$. This yields a diverging compressibility $\kappa \propto 1/\sqrt{\mu}$ around $\mu \simeq 0$. The latter is associated to a vacuum to TLL quantum phase transition [64]. Using Bose-Fermi mapping for the dilute gas, it may be understood as a van Hove singularity, which is induced by a diverging density of states at zero energy [65]. Finite-temperature effects smooth out this sharp edge of the density curves and eliminate the compressibility divergence. The latter is replaced at finite temperature by a maximum at finite chemical potential, which gets sharper as the temperature decreases. Comparing these results with those for the TG model, we find that both models exhibit qualitatively similar behaviors but significant quantitative differences. As expected, the TG and HR models agree in the low-density limit $na \ll 1$. However, significant deviations occur as the chemical potential increases due to the finite-separation impenetrability of the HR model. As a result, the compressibility of HRs is generically lower than that of the TG gas. Moreover, results not shown here indicate that these deviations are stronger when the temperature increases owing to the different excitation spectra of the HR and TG models. Note that, as anticipated, no simple proportional relation between the HR and TG models exists because the rescaling of energies and chemical potentials are different and depend on density and temperature.

IV. CORRELATION FUNCTIONS

Our results allow us to predict (up to numerical prefactors) the behavior of correlation functions assuming TLL behavior. For instance, using mode expansions of the TLL fields, the asymptotic one-body correlation function $g_1(x) = \langle\psi^\dagger(x)\psi(0)\rangle/n$ may be written, for $x \gg n^{-1}$, as [29]

$$g_1(x) = \sum_{m\geqslant 0} B_m \frac{\cos(2\pi nmx)}{|nd(x)|^{2m^2K+1/2K}}, \tag{20}$$

where K is the TLL parameter and $d(x) = \frac{L_T}{\pi}\sinh(\frac{\pi x}{L_T})$ is the thermal chord distance, with $L_T = \hbar u/k_BT$ the thermal length and u the speed of sound. A similar formula is found for the pair correlation function $g_2(x) = \langle\psi^\dagger(0)\psi^\dagger(x)\psi(x)\psi(0)\rangle/n^2$, which reads as

$$g_2(x) = 1 - \frac{2K}{|2\pi nd(x)|^2} + \sum_{m\geqslant 1} A_m \frac{\cos(2\pi nmx)}{|nd(x)|^{2m^2K}}. \tag{21}$$

For HRs, the speed of sound may be computed from the exact dispersion relation (13), which yields

$$u = \frac{\mathrm{d}\varepsilon}{\hbar \mathrm{d}q}\bigg|_{q=0} = \frac{\pi\hbar n}{m(1-na)^2}, \tag{22}$$

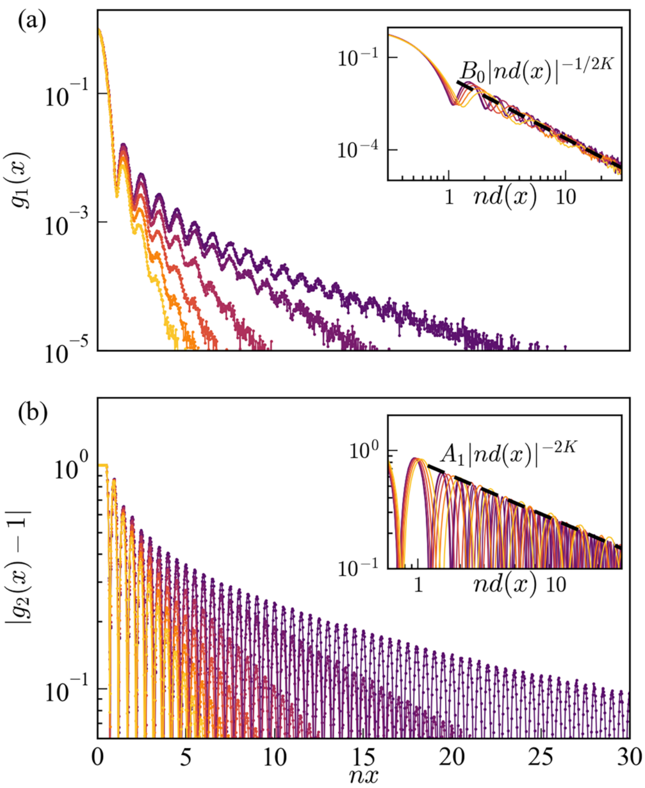

FIG. 3. Correlations in the HR model. (a) One-body correlation function $g_1(x)$ and (b) Pair correlation function $g_2(x)$ for $na = 0.5$ and various temperatures, in semilogarithmic scale. Solid lines are QMC results with temperatures $(k_B ma^2/\hbar^2)T = 0.1, 0.2, 0.4, 0.6, 0.8, 1.0$ from top (dark purple) to bottom (light yellow), corresponding to $nL_T = 31.4, 15.7, 7.86, 5.24, 3.93, 3.15$, respectively. The insets show the same data as in the main panels but plotted vs the thermal chord distance $d(x)$ in a log-log scale, and the dashed lines indicate the leading term of TLL predictions, Eqs. (20) and (21), where B_0 and A_1 are fitted parameters and K is computed using Eq. (23).

and the TLL parameter is given by [66]

$$K = \hbar k_F/mu = (1 - na)^2. \tag{23}$$

The nonuniversal (model-dependent) coefficients B_m and A_m are, however, not determined by the TLL theory. Figure 3 shows the complete correlation functions $g_1(x)$ and $|g_2(x) - 1|$ as computed using QMC for $na = 0.5$ and increasing temperatures (from top to bottom). We plot $|g_2(x) - 1|$ instead of $g_2(x)$, to highlight the oscillations. The main panels show the correlation functions plotted in semilogarithmic scale versus the distance x and the insets show the same data plotted in log-log scale versus the thermal chord distance $d(x)$. The plateau visible in the main panel of (b) for $nx < na = 0.5$, where $g_2(x) = 0$ ($|g_2(x) - 1| = 1$), is a result of the fully impenetrable nature of HRs. The asymptotic behaviors are consistent with Eqs. (20) and (21). In particular, both $g_1(x)$ and $g_2(x)$ exhibit oscillations versus x with period $1/n$, irrespective of temperature, and decay stronger with increasing temperature, consistently with $L_T \propto 1/T$ (see main panels in Fig. 3). For $x \ll L_T$, we find power-law decay reminiscent of the universal zero-temperature TLL behavior, while for $x \gg L_T$, we have $d(x) \sim \exp(\pi x/L_T)$ and exponential decay is found (the values of L_T are given in the caption of Fig. 3). Such a crossover is found in both $g_1(x)$ and $|g_2(x) - 1|$. Note that due to a relative decay factor $|nd(x)|^{-2K}$, the dominating $m = 1$ oscillations of $g_1(x)$ are suppressed with respect to the $m = 0$ term in Eq. (20) at large distance and high temperature. More precisely, universal algebraic decay (up to oscillations) with respect to $d(x)$ is expected. This is verified in the inset of Fig. 3(a), which shows $g_1(x)$ versus $d(x)$ in log-log scale for the same temperatures as in the main panel, and the dashed line denotes the leading ($m = 0$) term of Eq. (20), with K as given by Eq. (23) and B_0 as a fitting parameter. We find all curves collapse up to the oscillations, in agreement with the TLL predictions. Similarly, the inset of Fig. 3(b) shows $|g_2(x) - 1|$ versus $d(x)$ in log-log scale. The dominating term is the absolute value of the $m = 1$ oscillation. Since $K < 1$ for HRs, a universal power-law upper bound $A_1|nd(x)|^{-2K}$ is observed in this case, as indicated by the dashed line, which once again confirms the TLL predictions.

To further assess the TLL behavior, we now proceed with fits of Eqs. (20) and (21), up to the $m = 1$ terms, to the QMC data for various values of na. This allows us to extract K, L_T, and the coefficients B_0, B_1, and A_1. Furthermore, for $g_2(x)$, we fit the density n from the frequency of oscillations. We use a Levenberg-Marquardt least-square approach [67] in two steps. In the first step, we fit $g_1(x)$ and obtain estimates for K, B_0, and B_1. The thermal length L_T is, however, poorly estimated because thermal effects are only significant at large enough distance, $x \gtrsim L_T$, where the value of the correlation function is small and does not contribute much to the fit. To enhance the weight of the tails, we perform a second fit, now of $\ln[g_1(x)]$, using the previous estimates for K, B_0, and B_1, and fitting the parameter L_T only. The speed of sound u can then be extracted knowing the temperature, here $\tilde{T} = ma^2 k_B T/\hbar^2 = 0.01$ for $na \leqslant 0.1$, $\tilde{T} = 0.1$ for $0.13 \leqslant na \leqslant 0.6$, and $\tilde{T} = 0.9$ for $0.5 \leqslant na \leqslant 0.7$, respectively. These temperatures are chosen so that the system always remains in the LL regime, i.e., in a regime in which the nonlinear part of the excitation spectrum can be neglected. This condition is fulfilled when $k_B T$ does not exceed $\hbar^2\pi^2 n^2/2m(1 - na)^2$. Due to convergence issues, the extension to $na \gtrsim 0.6$ is more feasible for the highest temperature. A similar analysis is carried out for $g_2(x)$. In the first step, we fit $g_2(x)$ to obtain estimates of K, n, and A_1. For $na \geqslant 0.5$, we also include A_2 into the fits since this term becomes significant. In the second step, we fit all local maxima of $\ln|g_2(x) - 1|$ to extract L_T in order to exclude the points with $g_2(x) \approx 1$, which would otherwise yield large values of $\ln|g_2(x) - 1|$ and strongly affect the fits. For all cases, we find excellent agreement between the fitted curves and the QMC data (see examples in Appendix D).

The results of the fits are shown in Fig. 4, with error bars estimated by the residual sum of squares. Purple, blue, and green data correspond to fits of g_1 for the three different temperatures, while red and orange data correspond to fits of g_2 for the higher two temperatures. We find very good agreement with TLL theory for the parameter K obtained by fitting $g_1(x)$, except for a few points with $na \lesssim 0.2$, where the agreement is worse, but still fair with deviations less than 13%. The deviation at small values of na is due to the fact that dilute density leads to weak oscillations, which are

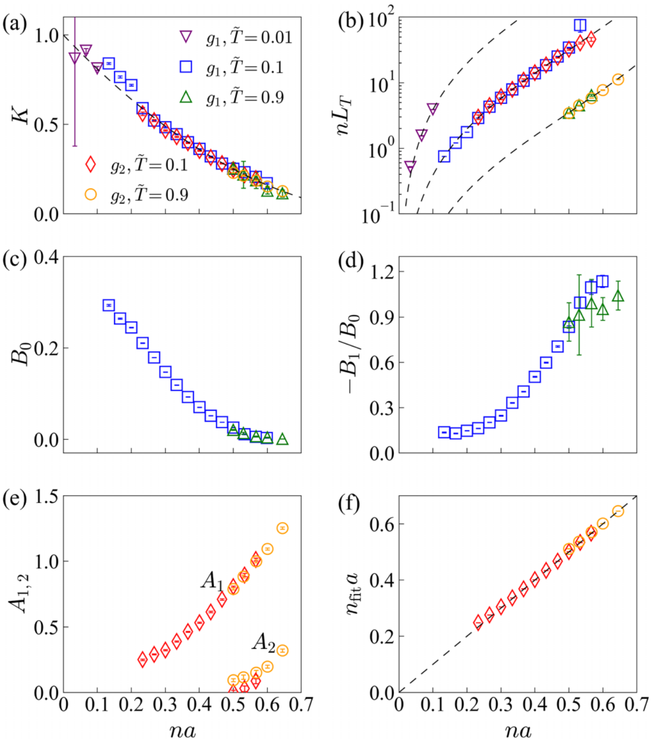

FIG. 4. Results of correlation function fits. We fit the TLL predictions, Eqs. (20) and (21), to QMC results, for $\tilde{T} = ma^2k_BT/\hbar^2 = 0.01$ (purple triangles), 0.1 (blue squares and red diamonds), and $\tilde{T} = 0.9$ (green triangles and orange circles). For $g_1(x)$, we take K, L_T, B_0, and B_1 as fitting parameters, and for $g_2(x)$, K, L_T, n, and A_1. Error bars are found to be smaller than the markers. The black dashed lines indicate TLL theory predictions. In (b) the three dashed lines indicate the thermal lengths for the considered temperatures.

further suppressed exponentially by finite temperature. The correlation function $g_1(x)$ approaches a pure exponential decay proportional to $\exp(-\pi x/2KL_T)$. The latter depends on KL_T, rather than K and L_T independently, leading to poor fitting of K. For $na \lesssim 0.1$, the oscillations are actually invisible, and the exponential decay renders the contribution of B_1 negligible in the fitting. It results in large uncertainties and the corresponding fits of B_0 and B_1/B_0 are not shown. Nevertheless, the behaviors of our results are consistent with the TG limit for $na \to 0$, with $K \to 1$, $nL_T \sim (na)^2$ [note the semilogarithmic scale in Fig. 4(b)], and the exact coefficients $B_0 \approx 0.52$ and $-B_1/B_0 \approx 1/8 = 0.125$ [27]. Similarly, for g_2, the weak amplitude and rapid decay of the oscillations allow less than two oscillation periods to be resolved before they are overwhelmed by statistical fluctuations, making a reliable fit impossible for $na \leqslant 0.2$. In the range $0.2 \lesssim na$, the estimates for K from $g_2(x)$ show good agreement with TLL theory, confirming the TLL theory predictions. Moreover, in the overlap region of $\tilde{T} = 0.1$ and 0.9, $0.5 \lesssim na \lesssim 0.6$, all fits agree well, confirming that the parameter K and all fitted coefficients are independent of T, thus validating the TLL predictions again.

The fits for L_T, as obtained in the second fit step, are also in good agreement with the TLL prediction, except for $na \gtrsim 0.5$–0.6. In this regime, the small value of K leads to fast decay of g_1 [see Eq. (20)], hiding the thermal effects under statistical fluctuations. Then, we cannot fit $g_1(x)$ for L_T although the fits for K obtained in the first fit still work well in this regime since they are not affected by the large value of L_T. In contrast, the oscillations of $g_2(x)$ decay slower because the $2K$ exponent is smaller than the exponent $1/2K + 2K$ of g_1 for $m = 1$, especially for large values of na. The valid range is larger against the QMC statistical fluctuations. Thus, we are able to fit L_T from g_2 in a larger range to obtain good estimates of L_T.

The quality of the fits for K and L_T, which yield results in very good agreement with the theoretical predictions, validates the reliability of the extracted coefficients B_0, B_1, A_1, and A_2. The increase in B_1/B_0, A_1, and A_2 indicates an enhancement of HRs solidification-like behavior. Furthermore, fits for n are shown in Fig. 4(f). We find that n_{fit} agrees with n perfectly, validating the predicted period of oscillation. Finally, we turn to the static structure factor $S(q) = \frac{1}{N}[\langle\rho_q\rho_{-q}\rangle - |\langle\rho_q\rangle|^2]$ where $\rho_q = \sum_{j=1}^{N} e^{-iqx_j}$. It is related to the pair correlation function through a Fourier transform,

$$S(q) = 1 + n\int_{-\infty}^{\infty} \mathrm{d}x[g_2(x) - 1]e^{iqx}. \tag{24}$$

For HRs at zero temperature, it was shown earlier that nonanalytical diverging peaks of $S(q)$ appear at $q = 2mk_F$ when $2m^2K < 1$, arising from the mth summation term in Eq. (21) [18,60,68]. At finite temperature, since the correlations turn to exponential decay for $x \gg L_T$, the behavior of the mth peak, $S_m = S(q \simeq 2mk_F)$, changes accordingly. Inserting Eq. (21) into Eq. (24), we find power-law scaling with temperature,

$$S_m - 1 \approx \frac{A_m\Gamma\left(\frac{1}{2} - m^2K\right)\Gamma(m^2K)}{2\sqrt{\pi}}\left(\frac{nL_T}{\pi}\right)^{1-2m^2K} + C, \tag{25}$$

where we collect the contributions of the terms other than $q = 2mk_F$ into a constant C. This leads to the scaling with thermal length $S_m - 1 \propto L_T^{1-2m^2K}$. Note that, for a finite-size system with size L, at zero temperature, the thermal length is replaced by the system size L, which yields the scaling $S_m(T = 0) - 1 \propto L^{1-2m^2K}$, consistent with the scaling with N found in Ref. [18]. It shows that $S_m(T = 0)$ scales up with increasing L for $1 - 2m^2K > 0$. At finite temperature, the nonanalytical peak present at zero temperature is replaced by a local maximum as indicated by Eq. (25), the height of which scales down with temperature as $S_m - 1 \propto 1/T^{1-2m^2K}$ since $L_T \propto 1/T$. The mth peak emerges when $na > 1 - 1/\sqrt{2m^2}$, which corresponds to $na > 0.293$ for the first peak ($m = 1$) and to $na > 0.646$ for the second peak ($m = 2$). Such peaks indicate the existence of a quasi-solid regime at high densities. The observed diverging $S(q)$ signals the onset of quasi-solid behavior, implying the enhancement of zero-energy modes at finite momentum. This is reminiscent of the supersolids in higher dimensions [69,70], where the softened roton gives rise to true long-range order. However, due to the reduced dimensionality here, although the ordering is significantly enhanced, it does not develop into true long-range order, and the system continues to fall within the TLL regime. In contrast, such peaks do not appear in the Lieb-Liniger model.

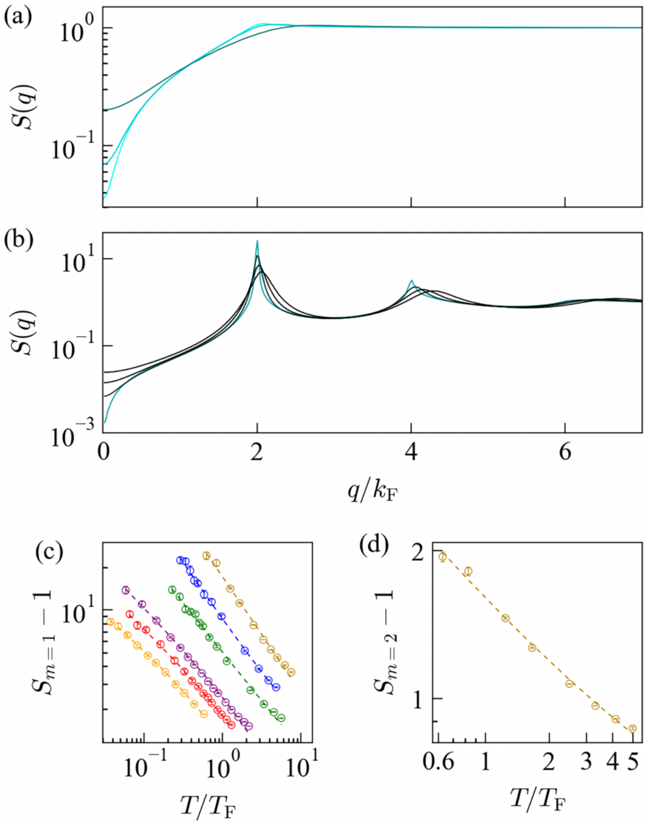

FIG. 5. Finite-temperature static structure factor $S(q)$ obtained from QMC computations at (a) $na = 0.1$ and temperatures $T/T_\mathrm{F} = 0.101$, 0.203, and 0.608, and (b) at $na = 0.7$ and $T/T_\mathrm{F} = 0.339$, 1.24, 1.65, 3.31, and 6.20, plotted from light to dark colors, where $T_\mathrm{F} = E_\mathrm{F}/k_\mathrm{B}$ is the Fermi temperature. The lower panels show the amplitude of the first peaks, (c) $S_{m=1}$ for various values of na and (d) $S_{m=2}$ for $na = 0.7$, vs temperature in log-log scale. Dashed lines are fitted power-law scalings, shifted by a constant C as given in Eq. (25), with fitted parameters and corresponding na shown in Table I.

TABLE I. Fits for $S_m(T)$.

na	m	K_BA	K_fit	A_m	C
0.47	1	0.2844	0.28(2)	0.70(12)	−1.1(5)
0.5	1	0.25	0.25(2)	0.76(14)	−0.7(4)
0.53	1	0.2209	0.227(12)	0.89(10)	−0.70(3)
0.6	1	0.16	0.15(3)	0.9(3)	0.1(4)
0.65	1	0.1225	0.09(4)	0.6(6)	0.5(9)
0.7	1	0.09	0.10(5)	1.6(17)	−0.2(15)
0.7	2	0.09	0.06(2)	0.16(10)	0.3(2)

The static structure factors at $na = 0.1$ and $na = 0.7$ for various temperatures are shown in Figs. 5(a) and 5(b), respectively, where lighter colors indicate lower temperatures. For $na = 0.1$, no peaks nor divergences are observed, consistently with the fact that $1 - 2K < 0$. In contrast, for $na = 0.7$, the first and second sharp peaks around $q = 2k_\mathrm{F}$ and $q = 4k_\mathrm{F}$, respectively, are clearly visible, consistently with the fact that $1 - 2m^2K > 0$ for $m = 1$ and $m = 2$. The peaks exhibit Lorentzian-like forms, with amplitudes that decrease with increasing temperature, implying that the quasi-solid ordering is weakened by thermal fluctuations. Meanwhile, the position of the peak slightly shifts toward larger momenta. This is consistent with the shift of the oscillating period of $g_2(x)$ observed at these temperatures (not shown here). The power-law scaling of the peak amplitudes S_m, Eq. (25), is confirmed in Figs. 5(c) and 5(d) for $m = 1$ and $m = 2$, respectively. Both clearly show linear scalings in log-log scale, consistent with Eq. (25). More precisely, we fit Eq. (25) to the data, with K, A_m, and C as fitting parameters. The QMC data for S_m (dots), together with the fits (dashed lines) are shown for various values of na, with fitted parameters given in Table I, where $K_\mathrm{BA} = (1 - na)^2$ is the BA prediction. We performed the fits in the range for $na \geqslant 0.47$, where the first peak is sufficiently large. We find good agreement for the $m = 1$ peaks, with relative discrepancy of K_fit less than 6% for $na \leqslant 0.6$. Furthermore, the value of A_1 at $na = 0.5$ agrees with the result of $g_2(x)$, and $A_1 \approx 1$ at $na = 0.6$ agrees with the result found at zero temperature in Ref. [18]. For $na \gtrsim 0.65$, the large density prevents QMC from converging at relatively lower temperatures and thus it is difficult to reach larger values of S_m [71]. Finally, the $m = 2$ peak is identified at $na = 0.7$ and the scaling relation is observed [see Fig. 5(d)]. Although the fit is worse than those of $S_{m=1}$, it still has a correct order of magnitude. In all simulations, the particle number is larger than 200. These results further confirm the TLL behavior of HRs at finite temperature.

V. CONCLUSION AND DISCUSSION

In conclusion, we reported the investigation of the thermodynamics of the one-dimensional HR gas. This model shows significant deviations compared to the Lieb-Liniger model, which corresponds to contact interactions, in regimes with relatively high density. By comparing the TBA solution and universal TLL predictions with QMC calculations for thermodynamic properties and correlation functions, we found excellent agreement. Our findings highlight the universal TLL behavior of the HR model across a wide range of parameters, as evidenced by correlation functions and static structure factors. We have shown that the parameters of the TLL model, K and u, can be extracted from fits of correlation functions. More precisely, we obtained the thermal length $L_T = \hbar u/k_\mathrm{B}T$, from which the speed of sound u can be deduced given the temperature T. Conversely, the same approach can be used to infer the temperature from the analytical value of the speed of sound. This makes the approach useful for thermometry in experiments. Furthermore, the numerical coefficients B_0, B_1, and A_1, which are unknown in the TLL approach, can also be extracted. An interesting direction for future studies would be to compute the dynamical structure factor at finite temperatures, which is of experimental relevance for instance in ultracold-atom systems.

Rydberg atom systems [72,73] may offer a promising platform to implement approximations of the HR model we have discussed in this paper. The bare van der Waals interactions already provide a sharp decay of interactions as the sixth power of the interatomic distance r, showing hard-core behavior of correlation functions on lattices [74]. This can be further improved using Rydberg dressing of the ground state, with effective interactions showing a plateau with a sharp $1/r^6$

decay [75–78] or even sharper via the electromagnetically induced transparency [79,80], and controlling of the width and height of the plateau controlled via the intensity and detuning of the coupling lasers. The excitation spectrum could then be measured using, for instance, quench spectroscopy [81–86] as recently implemented in Rydberg atom experiments [87]. Furthermore, thermodynamic properties may be studied by varying the interaction range a and/or the temperature by controlling the cooling ramp. Further investigation is deserved to assess the accuracy of such implementations in realizing the HR model.

ACKNOWLEDGMENTS

We thank Antoine Browaeys, Jacopo De Nardis, Dean Johnstone, and Zoran Ristivojevic for fruitful discussions. We acknowledge the CPHT computer team for valuable support. This research was supported by the Agence Nationale de la Recherche (ANR; Projects No. ANR-CMAQ-002 and No. ANR-23-PETQ-0002 France 2030), the IPParis Doctoral School, and HPC/AI resources from GENCI-TGCC (Grant No. 2023-A0110510300) using the ALPS scheduler library and statistical analysis tools [88,89].

DATA AVAILABILITY

The data that support the findings of this article are not publicly available. The data are available from the authors upon reasonable request.

APPENDIX A: NUMERICAL SOLUTION OF THE YANG-YANG EQUATION

To solve the Yang-Yang equation, Eq. (16), for HRs, we first rewrite it as

$$\epsilon(k) = -\mu + \frac{\hbar^2 k^2}{2m} + k_{\rm B}Ta \int \frac{{\rm d}k'}{2\pi} \ln[1 + e^{-\epsilon(k')/k_{\rm B}T}], \quad \text{(A1)}$$

using $K(k - k') = a$. Note that the integral depends on the yet unknown form of the function $\epsilon(k)$ but, contrary to the Lieb-Liniger case, is a constant, independent of k. It is then fruitful to rewrite it as

$$\epsilon(k) = -\mu + \frac{\hbar^2 k^2}{2m} + k_{\rm B}T\chi_1(\mu, T), \quad \text{(A2)}$$

with

$$\chi_1(\mu, T) = a \int \frac{{\rm d}k'}{2\pi} \ln[1 + e^{-\epsilon(k')/k_{\rm B}T}], \quad \text{(A3)}$$

which explicitly shows that $\epsilon(k)$ is a quadratic function of k. Inserting Eq. (A2) into Eq. (A3), we then find the self-consistent equation

$$\chi_1(\mu, T) = -\frac{a}{\lambda_T}{\rm Li}_{3/2}(-e^{\mu/k_{\rm B}T - \chi_1}), \quad \text{(A4)}$$

where ${\rm Li}_{3/2}$ is the polylogarithm function and $\lambda_T = \sqrt{2\pi\hbar^2/mk_{\rm B}T}$ is the thermal de Broglie wavelength. The right-hand-side term is a strictly decreasing function of χ_1, from a positive value for $\chi_1 = 0$ to zero for $\chi_1 \to \infty$. Equation (A4) has thus a unique solution for each value of μ and T, which is easily found using an iterative Newton method. Inserting the result into Eq. (A2), we then find $\epsilon(k)$.

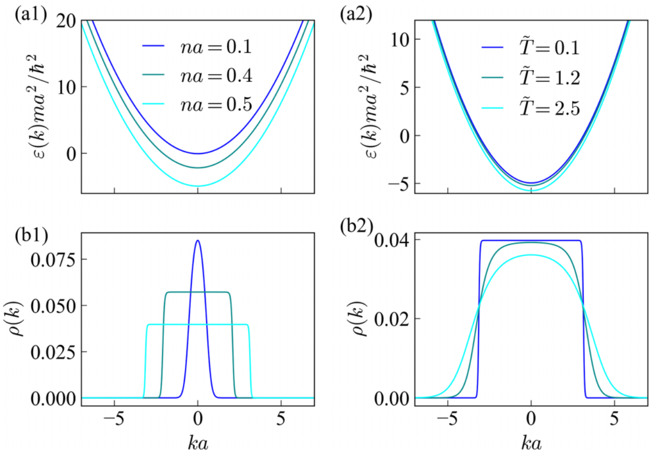

FIG. 6. (a) Dressed energy and (b) density of quasimomenta. Left: Various values of na for $T = 0.1\hbar^2/ma^2k_{\rm B}$. Right: Various temperatures for $na = 0.5$

After solving the Yang-Yang equation for $\epsilon(k)$, we can compute a number of quantities, including the quasimomentum density, given by $\rho(k) = \frac{1-na}{2\pi}\frac{1}{1+e^{\epsilon(k)/k_{\rm B}T}}$ [see Eq. (B2) in Appendix B]. Examples of the dressed energy $\epsilon(k)$ and the corresponding $\rho(k)$ are shown in Fig. 6. As expected, we find quadratic behavior of $\epsilon(k)$ as a function of k, and the Fermi-distribution-like density of quasimomenta. Note that $\rho(k)$ is not the momentum distribution, which equals the Fourier transform of the off-diagonal one-body density matrix.

APPENDIX B: DERIVATION OF THE DENSITY AND COMPRESSIBILITY

To find the density, we first write

$$\rho_h(k) = e^{\epsilon(k)/k_{\rm B}T}\rho(k), \quad \text{(B1)}$$

using Eq. (15). Since $\mathcal{K}(k) = a$ and $n = \int dk\rho(k)$, Eq. (14) reduces $\rho(k) + \rho_h(k) = \frac{1-na}{2\pi}$, and one finds

$$\rho(k) = \frac{1 - na}{2\pi}\frac{1}{1 + e^{\epsilon(k)/k_{\rm B}T}}. \quad \text{(B2)}$$

Then, integrating over k on both sides, one finds

$$n = (1 - na)\frac{\chi_2(\mu, T)}{a}, \quad \text{(B3)}$$

with $\chi_2(\mu, T) = a\int_{-\infty}^{\infty}\frac{{\rm d}k}{2\pi}\frac{1}{1+e^{\epsilon(k)/k_{\rm B}T}}$. Solving for n, one then finds Eq. (18).

The compressibility is found by differentiating Eq. (18) with respect to μ, which yields

$$\kappa = \left(\frac{\partial n}{\partial \mu}\right)_T = \frac{1}{a}\frac{1}{(1 + \chi_2)^2}\frac{\partial \chi_2(\mu, T)}{\partial \mu}. \quad \text{(B4)}$$

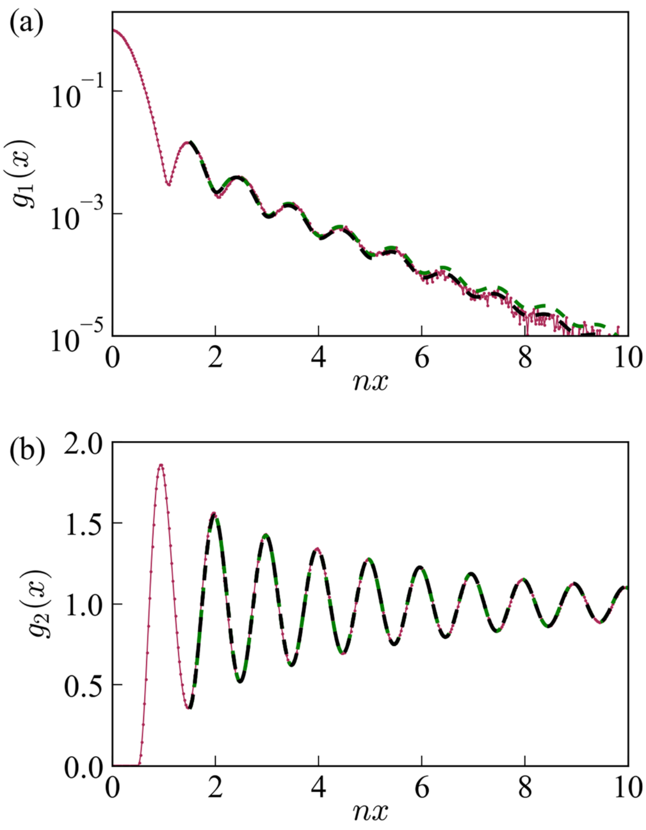

FIG. 7. Fits of correlation functions. The solid lines are $g_1(x)$ in panel (a) and $g_2(x)$ in panel (b) for $na = 0.5$ and $T = 0.4\hbar^2/ma^2k_\mathrm{B}$, while the dashed lines are the fitted curves at step one (dashed green line) and step two (dashed black line).

In addition, the definition of $\chi_2(\mu, T)$ leads to

$$\frac{\partial \chi_2(\mu, T)}{\partial \mu} = -\frac{a}{k_\mathrm{B}T}\int_{-\infty}^{\infty}\frac{\mathrm{d}k}{2\pi}\frac{e^{\epsilon(k)/k_\mathrm{B}T}}{[1 + e^{\epsilon(k)/k_\mathrm{B}T}]^2}\frac{\partial\epsilon(k)}{\partial\mu}. \tag{B5}$$

The Yang-Yang equation for HRs, Eq. (A2), yields

$$\frac{\partial\epsilon(k)}{\partial\mu} = -1 + k_\mathrm{B}T\frac{\partial\chi_1}{\partial\mu}, \tag{B6}$$

which is thus independent of k. Using Eq. (A3), we then find

$$\begin{aligned}\frac{\partial\epsilon(k)}{\partial\mu} &= -1 - a\int_{-\infty}^{\infty}\frac{\mathrm{d}k'}{2\pi}\frac{e^{-\epsilon(k')/k_\mathrm{B}T}}{1 + e^{-\epsilon(k')/k_\mathrm{B}T}}\frac{\partial\epsilon(k)}{\partial\mu}\\ &= -1 - \chi_2(\mu, T)\frac{\partial\epsilon(k)}{\partial\mu}\end{aligned} \tag{B7}$$

and, solving for $\partial\epsilon(k)/\partial\mu$, we find

$$\frac{\partial\epsilon(k)}{\partial\mu} = \frac{-1}{1 + \chi_2(\mu, T)}. \tag{B8}$$

Inserting Eq. (B8) into Eq. (B5), we get

$$\frac{\partial\chi_2(\mu, T)}{\partial\mu} = \frac{1}{k_\mathrm{B}T}\frac{\chi_3(\mu, T)}{1 + \chi_2(\mu, T)}, \tag{B9}$$

with $\chi_3(\mu, T) = a\int_{-\infty}^{\infty}\frac{\mathrm{d}k}{2\pi}\frac{e^{\epsilon(k)/k_\mathrm{B}T}}{(1+e^{\epsilon(k)/k_\mathrm{B}T})^2}$. Inserting this formula unto Eq. (B4) and using Eq. (B3), we finally find Eq. (19).

APPENDIX C: PROPAGATOR FOR QUANTUM MONTE CARLO

Here we derive the propagator for the QMC calculations. The path-integral Monte Carlo formulation in continuous space involves slicing the imaginary time into many small slices with imaginary time step τ. In each slice, the pair interaction propagator, i.e., the probability amplitude for the relative separation to move from x to x', is given by [90]

$$\begin{aligned}\rho^\mathrm{rel}(x, x', \tau) &= \sum_n \psi_n^*(x)e^{-\tau E_n/\hbar}\psi_n(x')\\ &\quad + \int_0^\infty \psi_k^*(x)e^{-\tau\hbar k^2/2m_\mathrm{rel}}\psi_k(x')\mathrm{d}k,\end{aligned} \tag{C1}$$

where $m_\mathrm{rel} = m/2$ is the reduced mass, $\psi_n(x)$ spans the set of bound states with energy E_n, and $\psi_k(x)$ spans the set of scattering states, for the reduced-particle Hamiltonian

$$H^\mathrm{rel} = -\frac{\hbar^2}{2m_\mathrm{rel}}\frac{\partial^2}{\partial x^2} + V(x). \tag{C2}$$

For HR interaction, there is no bound state and the scattering states are

$$\psi_k^\mathrm{s,a}(x) = \begin{cases}\frac{1}{\sqrt{\pi}}\sin{[k(x - a)]} & \text{for } x > a\\ \mp\frac{1}{\sqrt{\pi}}\sin{[k(x + a)]} & \text{for } x < -a\\ 0 & \text{otherwise.}\end{cases} \tag{C3}$$

The symmetric and antisymmetric states are denoted by the superscripts “s” and “a”, respectively. Substituting the expression of the scattering states, Eq. (C3), into Eq. (C1) we obtain

$$\rho(x, x', \tau) = \begin{cases}\sqrt{\frac{m}{4\pi\tau\hbar^2}}\left(e^{-[m(x-x')^2/4\tau\hbar^2]} - e^{-[m(|x+x'|-2a)^2/4\tau\hbar^2]}\right) & \text{for } xx' > 0 \text{ and } |x|, |x'| > a\\ 0 & \text{otherwise.}\end{cases} \tag{C4}$$

This analytic expression is directly implemented in the QMC numerical code.

APPENDIX D: FITS OF CORRELATION FUNCTIONS

Here we show a typical result of the fits of correlation functions. Figure 7 shows the one-body correlation function $g_1(x)$ and the pair correlation function $g_2(x)$ for $na = 0.5$ and $T = 0.4\hbar^2/ma^2k_\mathrm{B}$ as found by QMC calculations (red dots and lines), together with the corresponding fits (dashed green line for the first-step fit and dashed black line for the second-step fit). We find similarly good agreement for all fits performed for this work.

[1] J.-P. Hansen and I. R. McDonald, *Theory of Simple Liquids (*Elsevier Academic Press, New York, 2006).

[2] M. N. Rosenbluth and A. W. Rosenbluth, Further results on monte carlo equations of state, J. Chem. Phys. **22**, 881 (1954).

[3] J. C. Dyre, Simple liquids' quasiuniversality and the hard-sphere paradigm, J. Phys.: Condens. Matter **28**, 323001 (2016).

[4] Á. Mulero, *Theory and Simulation of Hard-Sphere Fluids and Related Systems* (Springer, New York, 2008), p. 753.

[5] J. K. Percus, Equilibrium state of a classical fluid of hard rods in an external field, J. Stat. Phys. **15**, 505 (1976).

[6] S. Olla and P. Ferrari, Diffusive fluctuations in hard rods system, arXiv:2210.02079.

[7] O. A. Castro-Alvaredo, B. Doyon, and T. Yoshimura, Emergent hydrodynamics in integrable quantum systems out of equilibrium, Phys. Rev. X **6**, 041065 (2016).

[8] B. Bertini, M. Collura, J. De Nardis, and M. Fagotti, Transport in out-of-equilibrium XXZ chains: Exact profiles of charges and currents, Phys. Rev. Lett. **117**, 207201 (2016).

[9] B. Doyon and H. Spohn, Drude weight for the Lieb-Liniger Bose gas, SciPost Phys. **3**, 039 (2017).

[10] L. Biagetti, G. Cecile, and J. De Nardis, Three-stage thermalization of a quasi-integrable system, Phys. Rev. Res. **6**, 023083 (2024).

[11] F. Hübner, L. Biagetti, J. De Nardis, and B. Doyon, Diffusive hydrodynamics of hard rods from microscopics, Sci-Post Physics Core **9**, 010 (2026).

[12] C. P. Royall, P. Charbonneau, M. Dijkstra, J. Russo, F. Smallenburg, T. Speck, and C. Valeriani, Colloidal hard spheres: Triumphs, challenges, and mysteries, Rev. Mod. Phys. **96**, 045003 (2024).

[13] J. V. Pearce, M. A. Adams, O. E. Vilches, M. R. Johnson, and H. R. Glyde, One-dimensional and two-dimensional quantum systems on carbon nanotube bundles, Phys. Rev. Lett. **95**, 185302 (2005).

[14] M. M. Calbi, M. W. Cole, S. M. Gatica, M. J. Bojan, and G. Stan, Condensed phases of gases inside nanotube bundles, Rev. Mod. Phys. **73**, 857 (2001).

[15] A. B. Michelsen, M. Valiente, N. T. Zinner, and A. Negretti, Ion-induced interactions in a Tomonaga-Luttinger liquid, Phys. Rev. B **100**, 205427 (2019).

[16] A. J. Vidal, G. E. Astrakharchik, L. V. Markic, and J. Boronat, One dimensional ^{1}H, ^{2}H and ^{3}H, New J. Phys. **18**, 055013 (2016).

[17] M. Rigol and A. Muramatsu, Emergence of quasicondensates of hard-core bosons at finite momentum, Phys. Rev. Lett. **93**, 230404 (2004).

[18] F. Mazzanti, G. E. Astrakharchik, J. Boronat, and J. Casulleras, Ground-state properties of a one-dimensional system of hard rods, Phys. Rev. Lett. **100**, 020401 (2008).

[19] G. E. Astrakharchik, J. Boronat, J. Casulleras, and S. Giorgini, Beyond the Tonks-Girardeau gas: Strongly correlated regime in quasi-one-dimensional Bose gases, Phys. Rev. Lett. **95**, 190407 (2005).

[20] G. De Rosi, G. E. Astrakharchik, and S. Stringari, Thermodynamic behavior of a one-dimensional Bose gas at low temperature, Phys. Rev. A **96**, 013613 (2017).

[21] G. De Rosi, P. Massignan, M. Lewenstein, and G. E. Astrakharchik, Beyond-Luttinger-liquid thermodynamics of a one-dimensional Bose gas with repulsive contact interactions, Phys. Rev. Res. **1**, 033083 (2019).

[22] M. L. Kerr, G. D. Rosi, and K. V. Kheruntsyan, Analytic thermodynamic properties of the Lieb-Liniger gas, SciPost Phys. Core **7**, 047 (2024).

[23] V. D. Naik, F. B. Trigueros, and M. Heyl, Quantum hard disks on a lattice, Phys. Rev. B **110**, L220303 (2024).

[24] E. H. Lieb and W. Liniger, Exact analysis of an interacting Bose gas. I. The general solution and the ground state, Phys. Rev. **130**, 1605 (1963).

[25] E. H. Lieb, Exact analysis of an interacting Bose gas. II. The excitation spectrum, Phys. Rev. **130**, 1616 (1963).

[26] T. Giamarchi, *Quantum Physics in One Dimension* (Carendon, Oxford, 2004).

[27] M. A. Cazalilla, R. Citro, T. Giamarchi, E. Orignac, and M. Rigol, One dimensional bosons: From condensed matter systems to ultracold gases, Rev. Mod. Phys. **83**, 1405 (2011).

[28] F. D. M. Haldane, Solidification in a soluble model of bosons on a one-dimensional lattice: The Boson-Hubbard chain, Phys. Lett. A **80**, 281 (1980).

[29] F. D. M. Haldane, Effective harmonic-fluid approach to low-energy properties of one-dimensional quantum fluids, Phys. Rev. Lett. **47**, 1840 (1981).

[30] T. Giamarchi, Mott transition in one dimension, Phys. B (Amsterdam, Neth.) **230-232**, 975 (1997).

[31] T. Giamarchi and H. J. Schulz, Localization and interactions in one-dimensional quantum fluids, Europhys. Lett. **3**, 1287 (1987).

[32] T. Giamarchi and H. J. Schulz, Anderson localization and interactions in one-dimensional metals, Phys. Rev. B **37**, 325 (1988).

[33] J. Vidal, D. Mouhanna, and T. Giamarchi, Interacting fermions in self-similar potentials, Phys. Rev. B **65**, 014201 (2001).

[34] G. Roux, T. Barthel, I. P. McCulloch, C. Kollath, U. Schollwöck, and T. Giamarchi, Quasiperiodic Bose-Hubbard model and localization in one-dimensional cold atomic gases, Phys. Rev. A **78**, 023628 (2008).

[35] T. Roscilde, Bosons in one-dimensional incommensurate superlattices, Phys. Rev. A **77**, 063605 (2008).

[36] H. Yao, H. Khoudli, L. Bresque, and L. Sanchez-Palencia, Critical behavior and fractality in shallow one-dimensional quasiperiodic potentials, Phys. Rev. Lett. **123**, 070405 (2019).

[37] H. Yao, T. Giamarchi, and L. Sanchez-Palencia, Lieb-Liniger bosons in a shallow quasiperiodic potential: Bose glass phase and fractal Mott lobes, Phys. Rev. Lett. **125**, 060401 (2020).

[38] T. Kinoshita, T. Wenger, and D. S. Weiss, Observation of a one-dimensional Tonks-Girardeau gas, Science **305**, 1125 (2004).

[39] B. Paredes, A. Widera, V. Murg, O. Mandel, S. Fölling, I. Cirac, G. V. Shlyapnikov, T. W. Hänsch, and I. Bloch, Tonks-Girardeau gas of ultracold atoms in an optical lattice, Nature (London) **429**, 277 (2004).

[40] T. Kinoshita, T. Wenger, and D. S. Weiss, A quantum Newton's cradle, Nature (London) **440**, 900 (2006).

[41] C. Kim, A. Y. Matsuura, Z.-X. Shen, N. Motoyama, H. Eisaki, S. Uchida, T. Tohyama, and S. Maekawa, Observation of spin-charge separation in one-dimensional SrCuO$_2$, Phys. Rev. Lett. **77**, 4054 (1996).

[42] B. Kim, H. Koh, E. Rotenberg, S.-J. Oh, H. Eisaki, N. Motoyama, S.-i. Uchida, T. Tohyama, S. Maekawa, Z.-X. Shen, *et al.*, Distinct spinon and holon dispersions in photoemission spectral functions from one-dimensional $SrCuO_2$, Nat. Phys. **2**, 397 (2006).

[43] E. Haller, R. Hart, M. J. Mark, J. G. Danzl, L. Reichsöllner, M. Gustavsson, M. Dalmonte, G. Pupillo, and H.-C. Nägerl, Pinning quantum phase transition for a Luttinger liquid of strongly interacting bosons, Nature (London) **466**, 597 (2010).

[44] G. Boéris, L. Gori, M. D. Hoogerland, A. Kumar, E. Lucioni, L. Tanzi, M. Inguscio, T. Giamarchi, C. D'Errico, G. Carleo, *et al.*, Mott transition for strongly interacting one-dimensional bosons in a shallow periodic potential, Phys. Rev. A **93**, 011601(R) (2016).

[45] H. Yao, L. Tanzi, L. Sanchez-Palencia, T. Giamarchi, G. Modugno, and C. D'Errico, Mott transition for a Lieb-Liniger gas in a shallow quasiperiodic potential: Delocalization induced by disorder, Phys. Rev. Lett. **133**, 123401 (2024).

[46] H. Yao, D. Clément, A. Minguzzi, P. Vignolo, and L. Sanchez-Palencia, Tan's contact for trapped Lieb-Liniger bosons at finite temperature, Phys. Rev. Lett. **121**, 220402 (2018).

[47] Q. Huang, H. Yao, X. Chen, and L. Sanchez-Palencia, Direct measurement of Tan's contact in a one-dimensional Lieb-Liniger gas, Sci. Adv. **11**(40), eadv3727 (2025).

[48] S.-i. Tomonaga, Remarks on Bloch's method of sound waves applied to many-fermion problems, Prog. Theor. Phys. **5**, 544 (1950).

[49] J. Luttinger, An exactly soluble model of a many-fermion system, J. Math. Phys. **4**, 1154 (1963).

[50] F. D. M. Haldane, Luttinger liquid theory of one-dimensional quantum fluids. I. Properties of the Luttinger model and their extension to the general 1D interacting spinless fermi gas, J. Phys. C **14**, 2585 (1981).

[51] S. R. White, Density-matrix algorithms for quantum renormalization groups, Phys. Rev. B **48**, 10345 (1993).

[52] U. Schollwöck, The density-matrix renormalization group, Rev. Mod. Phys. **77**, 259 (2005).

[53] U. Schollwöck, The density-matrix renormalization group in the age of matrix product states, Prog. Theor. Phys. **326**, 96 (2011).

[54] B. Sutherland, *Beautiful Models: 70 Years of Exactly Solved Quantum Many-Body Problems* (World Scientific, Singapore, 2004).

[55] T. Nagamiya, Statistical mechanics of one-dimensional substances I, in *Proceedings of the Physico-Mathematical Society of Japan, 3rd Series* 22, 705 (1940).

[56] B. Sutherland, Quantum many-body problem in one dimension: Ground state, J. Math. Phys. **12**, 246 (1971).

[57] B. Sutherland, Quantum many-body problem in one dimension: Thermodynamics, J. Math. Phys. **12**, 251 (1971).

[58] M. Wadati and G. Kato, One-dimensional hard-core Bose gas, Chaos, SolitonsFractals **14**, 23 (2002).

[59] L. Šamaj and Z. Bajnok, *Introduction to the Statistical Physics of Integrable Many-Body Systems* (Cambridge University Press, Cambridge, 2013).

[60] M. Motta, E. Vitali, M. Rossi, D. Galli, and G. Bertaina, Dynamical structure factor of one-dimensional hard rods, Phys. Rev. A **94**, 043627 (2016).

[61] M. Girardeau, Relationship between systems of impenetrable bosons and fermions in one dimension, J. Math. Phys. **1**, 516 (1960).

[62] C. N. Yang and C. P. Yang, Thermodynamics of a one-dimensional system of bosons with repulsive delta-function interaction, J. Math. Phys. **10**, 1115 (1969).

[63] M. Boninsegni, N. Prokof'ev, and B. Svistunov, Worm algorithm for continuous-space path integral Monte Carlo simulations, Phys. Rev. Lett. **96**, 070601 (2006).

[64] S. Sachdev, *Quantum Phase Transitions* (Cambridge University Press, Cambridge, UK, 2001).

[65] N. Ashcroft and N. Mermin, *Solid State Physics* (Saunders College Publishing, Philadelphia, 1976).

[66] M. A. Cazalilla, Bosonizing one-dimensional cold atomic gases, J. Phys. B **37**, S1 (2004).

[67] J. J. Moré, in *Numerical Analysis: Proceedings of the Biennial Conference* (Springer, New York, 2006), pp. 105–116.

[68] G. Astrakharchik and J. Boronat, Luttinger-liquid behavior of one-dimensional ^{3}He, Phys. Rev. B **90**, 235439 (2014).

[69] S. Saccani, S. Moroni, and M. Boninsegni, Excitation spectrum of a supersolid, Phys. Rev. Lett. **108**, 175301 (2012).

[70] L. Tanzi, S. Roccuzzo, E. Lucioni, F. Famá, A. Fioretti, C. Gabbanini, G. Modugno, A. Recati, and S. Stringari, Supersolid symmetry breaking from compressional oscillations in a dipolar quantum gas, Nature (London) **574**, 382 (2019).

[71] D. M. Ceperley, Path integrals in the theory of condensed helium, Rev. Mod. Phys. **67**, 279 (1995).

[72] A. Browaeys, D. Barredo, and T. Lahaye, Experimental investigations of dipole-dipole interactions between a few Rydberg atoms, J. Phys. B **49**, 152001 (2016).

[73] A. Browaeys and T. Lahaye, Many-body physics with individually controlled Rydberg atoms, Nat. Phys. **16**, 132 (2020).

[74] H. Labuhn, D. Barredo, S. Ravets, S. De Léséleuc, T. Macrí, T. Lahaye, and A. Browaeys, Tunable two-dimensional arrays of single rydberg atoms for realizing quantum ising models, Nature (London) **534**, 667 (2016).

[75] G. Pupillo, A. Micheli, M. Boninsegni, I. Lesanovsky, and P. Zoller, Strongly correlated gases of Rydberg-dressed atoms: Quantum and classical dynamics, Phys. Rev. Lett. **104**, 223002 (2010).

[76] J. Honer, H. Weimer, T. Pfau, and H. P. Büchler, Collective many-body interaction in Rydberg dressed atoms, Phys. Rev. Lett. **105**, 160404 (2010).

[77] J. E. Johnson and S. L. Rolston, Interactions between Rydberg-dressed atoms, Phys. Rev. A **82**, 033412 (2010).

[78] M. Płodzień, G. Lochead, J. de Hond, N. J. van Druten, and S. Kokkelmans, Rydberg dressing of a one-dimensional Bose-Einstein condensate, Phys. Rev. A **95**, 043606 (2017).

[79] C. Gaul, B. J. DeSalvo, J. A. Aman, F. B. Dunning, T. C. Killian, and T. Pohl, Resonant Rydberg dressing of alkaline-earth atoms via electromagnetically induced transparency, Phys. Rev. Lett. **116**, 243001 (2016).

[80] S. Helmrich, A. Arias, N. Pehoviak, and S. Whitlock, Two-body interactions and decay of three-level Rydberg-dressed atoms, J. Phys. B **49**, 03LT02 (2016).

[81] R. Menu and T. Roscilde, Quench dynamics of quantum spin models with flat bands of excitations, Phys. Rev. B **98**, 205145 (2018).

[82] R. Menu and T. Roscilde, Gaussian-state ansatz for the non-equilibrium dynamics of quantum spin lattices, SciPost Phys. **14**, 151 (2023).

[83] L. Villa, J. Despres, and L. Sanchez-Palencia, Unraveling the excitation spectrum of many-body systems from quantum quenches, Phys. Rev. A **100**, 063632 (2019).

[84] L. Villa, J. Despres, S. Thomson, and L. Sanchez-Palencia, Local quench spectroscopy of many-body quantum systems, Phys. Rev. A **102**, 033337 (2020).

[85] L. Villa, S. J. Thomson, and L. Sanchez-Palencia, Quench spectroscopy of a disordered quantum system, Phys. Rev. A **104**, L021301 (2021).

[86] L. Villa, S. J. Thomson, and L. Sanchez-Palencia, Finding the phase diagram of strongly correlated disordered bosons using quantum quenches, Phys. Rev. A **104**, 023323 (2021).

[87] C. Chen, G. Emperauger, G. Bornet, F. Caleca, B. Gély, M. Bintz, S. Chatterjee, V. Liu, D. Barredo, N. Y. Yao, *et al.*, Spectroscopy of elementary excitations from quench dynamics in a dipolar XY Rydberg simulator, Science **389**, 483 (2025).

[88] M. Troyer, B. Ammon, and E. Heeb, Parallel object oriented Monte Carlo simulations, Lect. Notes Comput. Sci. **1505**, 191 (1998).

[89] B. Bauer, L. D. Carr, H. Evertz, A. Feiguin, J. Freire, S. Fuchs, L. Gamper, J. Gukelberger, E. Gull, S. Guertler, *et al.*, The ALPS project release 2.0: Open source software for strongly correlated systems, J. Stat. Mech. (2011) P05001.

[90] Y. Yan and D. Blume, Incorporating exact two-body propagators for zero-range interactions into N-body Monte Carlo simulations, Phys. Rev. A **91**, 043607 (2015).